



OPEN

An exhaustive scrutiny to amplify the heating prospects by devising a core@shell nanostructure for constructive magnetic hyperthermia applications

S. P. Tsopoe¹, C. Borgohain², Manoranjan Kar³, Shantanu Kumar Panda³ & J. P. Borah^{1✉}

An interfacial integration at the nanoscale domain through a core@shell (CS) nanostructure has constructively unbarred a wide dimension to researchers on biomedical applications, especially for magnetic fluid hyperthermia. Lately, the interconnection of the exchange bias effect (EBE) through the interface coupling to the magnetic heating efficiency has uttered its utmost prominence for researchers. Here, we delineate the ascendancy of the heating ability through a coalescing assembly of mixed ferrite $\text{Co}_{0.5}\text{Zn}_{0.5}\text{Fe}_2\text{O}_4$ (CZ) and soft magnetic material Fe_3O_4 (F), by devising a network of $\text{CoZnFe}_2\text{O}_4@Fe_3O_4$ (CZF) CS nanostructure. A hefty interface activity with validation of the EBE phenomenon is divulged through magnetic scrutiny for the CS sample. The magnetic nanoparticles heating response to applied magnetic field and frequency is discerned at three distinct fields, where the outcome prevailed to inflated specific loss power for CS CZF in distinction to bare F and CZ samples for all the assessments. Remarkably; a lofty intrinsic loss parameter is also perceived for the CS sample recorded to about $5.36 \text{ nHm}^2 \text{ g}^{-1}$; which is another eccentric outcome that significantly labels the CS CZF sample as a potentially high heating competence agent. This comprehension accords to a finer perspective to meliorate the theranostic environment for hyperthermia applications.

Single-domain magnetic nanoparticles (MNPs) have become one of the potentially explored research which has gained gigantic attention in the field of biomedical applications^{1,2}. Hyperthermia, a cancer remedy through the heat generation on suspension of the MNPs in the tumor cells via AC magnetic field is one of the emerging fields of biomedicine applications. Unlike radiotherapy or chemotherapy, localized and selective targeting heating of tumor cells is designed to even at low dosages of MNPs for hyperthermia which is carried out at shorter time regimes as well. Higher dosages of MNPs will regard to toxicity which results in potential side effects for directed cancer therapy. Hyperthermia efficiency is entirely associated with specific loss power (SLP), which regards the quantity of heat released by MNPs per unit mass. Therefore, the therapeutic need is to secure a maximum SAR value with minimal concentration that will outstretch to threshold temperature ($42\text{--}46 \text{ }^\circ\text{C}$)³⁻⁶. Indeed, this therapy using MNPs has been effectively demonstrated in several cancer treatments such as prostate cancer, brain tumor, invasive breast carcinoma, etc^{7,8}. The past investigation prevailed that soft MNPs are preferable within the clinical limit of applied field and frequency for effective hyperthermia⁹. Iron-oxides MNPs are the most investigated materials for this cancer therapy, especially Fe_3O_4 and $\gamma\text{-Fe}_2\text{O}_3$ are proven to be non-toxic even at 1 mg/mL concentration which is competently tolerated by human tissues¹⁰⁻¹². However, despite the non-toxic property etiquette of Fe_3O_4 and $\gamma\text{-Fe}_2\text{O}_3$, their low SLP values and less chemical stability make them unpleasing for effective magnetic hyperthermia applications. Therefore, one must emphasize to improving the chemical stability and also enhancing the SLP value by tuning its magnetic properties. One such representation is a core@shell type nanostructure; where the presence of shell assists in tuning the magnetic properties of the core material due to their interface exchange coupling. Also; it is significant to account that, the presence of the shell not only tunes the magnetic properties but it amplifies the stability of the core material as well¹³. Another distinctive property originating from interface coupling is the exchange bias effect which manifests in enhancing coercivity

¹Department of Physics, National Institute of Technology Nagaland, Dimapur, Nagaland 797103, India. ²Central Instrumentation Facility (CIF), Indian Institute of Technology Guwahati, Guwahati 781039, India. ³Department of Physics, Indian Institute of Technology Patna, Patna, Bihar 801106, India. ✉email: jpborah@rediffmail.com

and repositioning of the hysteresis loop towards the field direction^{14–17}. Magnetic nanostructure exhibiting EBE has a great advantage in the field of biomedical applications as they can well stabilize and control in opposition to thermal fluctuations¹⁸. Presently, researchers are putting diverse attention to developing the interconnection between the EBE and the heating efficiency of MNPs. Recently, it was experimentally reported that the SLP value emerges proportionally to the strength of EBE value i.e. with a reduction in the strength of EBE; the SAR is hindered to a lesser value and vice-versa. Also, they have reported that an inverted CS counterpart is superior to the normal CS nanostructure endorsing to a better heating capability¹⁹. The magnetic interchange coupling at the interface of the CS nanostructure magnifies the heating ability of MNPs, no doubt. However, it is important to know as to which factor dominates more in the collaboration tuning of the magnetic properties through the coupling of core and shell material. Many theoretical, as well as experimental works have been executed and it is evident that the variation of the shell thickness is more significant in tuning the magnetic properties rather than performing a variation on the core thickness^{20,21}. Essentially, the heating aptitude of the MNP relies upon sundry ingredients such as effective anisotropy, particle size, and distribution, saturation magnetization, applied field and frequency, the viscosity of the solvent, etc^{22–25}. As described above, the shell performs a significant role in tuning the properties of the MNPs, and therefore; in this present work, we have chosen Fe₃O₄ as the shell material and Co_{0.5}Zn_{0.5}Fe₂O₄ as the core material, where the CS (Co_{0.5}Zn_{0.5}Fe₂O₄@Fe₃O₄) nanostructure is carefully produced by making use of co-precipitation method. Eventually, an investigation to bare CoFe₂O₄ and CoFe₂O₄@Fe₃O₄ (or Fe₃O₄@CoFe₂O₄) is widely explored, while to our comprehension, Co_{0.5}Zn_{0.5}Fe₂O₄@Fe₃O₄ CS nanostructure has not been scrutinized for magnetic hyperthermia applications. In this toil, we have performed a comparative study of both bare F and CZ material with the CS CZF material and it resulted to better heating efficiency for CS in comparison to single materials that remarkably entitled the sample as a befitting agent for magnetic hyperthermia applications.

Experimental

Ferric chloride (FeCl₃·6H₂O) (97%), Zinc chloride (ZnCl₂) (99.5%), ferrous chloride (FeCl₂·4H₂O) (98%), Sodium hydroxide (NaOH) (80%) and Cobalt chloride (CoCl₂·6H₂O) (97%) were utilized to prepare the CS sample Co_{0.5}Zn_{0.5}Fe₂O₄@Fe₃O₄. All the raw materials were acquired from merk and employed without further moderation.

A two-step co-precipitation strategy was employed to synthesize the CS Co_{0.5}Zn_{0.5}Fe₂O₄@Fe₃O₄ MNPs. At first, an amount of 1.57 g of FeCl₃·6H₂O, 0.806 g of CoCl₂·6H₂O, and 0.849 g of ZnCl₂ were liquefied at 50 mL Milli Q water and applied constant stirring for 30 min at 50 °C to homogenize the mixture. Also, during constant magnetic stirring, a solution of 1.07 g of NaOH dissolved in 15 mL Milli Q water was added drop-wise as a precipitating agent until pH was acquired to 12. After this, the magnetic solution was then heated and stirred continuously for 60 min for a suitable reaction at 80 °C. Then, a dark brown precipitate was cleansed multiple times with Milli Q water and ethanol for residual chloride removal. Lastly, the precipitate was kept at 80 °C for 12 h to dry where CZ MNPs were formed. In the following step, 3.12 g of FeCl₃·6H₂O, 1.24 g of FeCl₂·4H₂O, and 1 g of the already formed CZ grain powder were mixed in 50 mL Milli Q water to secure a certain definite molar concentration, followed by the same procedure described earlier in the first step. Finally, after washing several times with Milli Q water and ethanol, the sample was dried in the oven at 80 °C for 12 h and the dark brown sample was ground to fine powders by making use of a pestle and agate mortar, where CS CZF sample was acquired.

Result and discussions

XRD analysis. The XRD spectra manifested in Fig. 1a–c explicate the crystal structure and the vindication of crystal phase purity for (a) bare F, (b) bare CZ, and (c) CS CZF samples, respectively. The XRD peaks emanated for all three samples ensure an fcc structure which is in concurrence with the standard JCPDS cards; 22-1086 with Fd3m space group for C sample, 89-3854 and 89-1010 for F and Z, both endorsing an Fd3m space group, respectively. No other supplementary peaks are observed in the XRD spectra expounding the crystal phase purity of the as-synthesis samples. The FWHM (Full-Width Half-Maxima) of the fiercest peaks of the spectra were optimized, through which the mean crystallite sizes were estimated using Scherrer's formula²⁶. The evaluated mean crystallite size and the respective lattice constants for all the samples are lay-out in Table 1.

Microstructure analysis. Figure 2a–c lay out the typical TEM micrographs along with their respective plotted particle sizes histogram for samples F, CZ, and CFZ, respectively. Figure 2a,b ensues a non-uniform distribution of MNPs with spheroids shape for the bare samples F and CZ, while the CS sample displayed in Fig. 2c exhibits similar shape but agglomerated NPs. Agglomeration of NPs might occur through the Brownian mechanism where the NPs are attached under their random motion and also due to the gravitational effect which is dependent on the thermal speed and the particle size²⁷. However, the TEM image along with the inset shown in Fig. 2c authenticates a CS nanostructure. The average associated particle sizes obtained through the fitted histogram are 8.36 ± 3 nm, 6.99 ± 2 nm, and 9.86 ± 3 nm for F, CZ, and CZF respectively. The enhanced particle size for the CS sample might result due to higher polydispersity originating through the second step synthesis procedure involved²⁸. The average shell thickness for the CS sample is evaluated with its mean size of about 1.89 ± 0.32 nm.

Figure 3a–c present the HRTEM micrographs with their respective IFFT (Inverse Fast Fourier Transform) images validating the d-spacing value for F, CZ, and CZF samples. Figure 3a reveals the phase inclination for the (220) plane with its respective d-spacing value ($d_{220} = 0.296$ nm) for the bare F sample. Also, for the mixed ferrite CZ sample shown in Fig. 3b, the d-spacing value for C and Z are individually verified with the (111) plane for C ($d_{111} = 0.484$ nm) and (311) plane for Z ($d_{311} = 0.254$ nm), respectively. Further, for the CS sample CZF, the IFFT image was extracted from the premise of the CS interface capturing all the planes for C, Z, and F. The crystal planes for core sample CZ is identical as described above in Fig. 3b, while the shell sample F is authenticated to

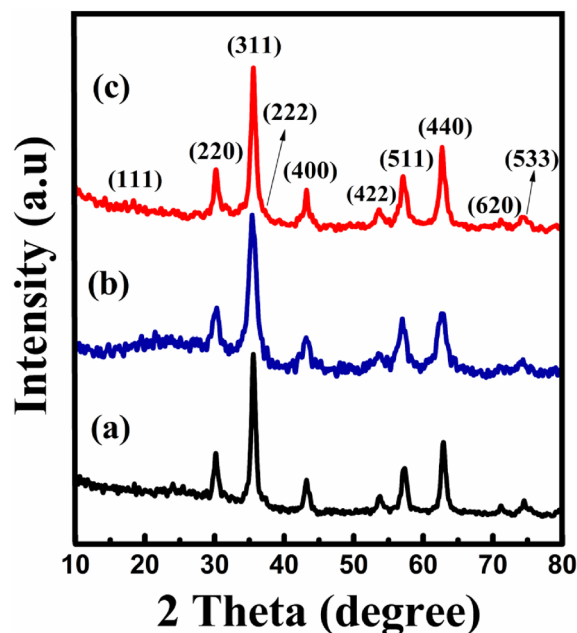


Figure 1. XRD spectra of (a) F, (b) CZ, and (c) CZF samples.

Sample	Crystallite size (nm)	Lattice constant (Å)
F	4.57	8.39
CZ	3.21	8.37
CZF	5.75	8.35

Table 1. Crystallite size and lattice constant of F, CZ, and CZF samples.

d-spacing value (0.485 nm) for (111) crystal plane. All the evident d-spacing values for C, Z, and F are verified with their respective JCPDS file no. describe in the XRD analysis.

Figure 4a–c convey the SAED spectra achieved by the MNPs displaying concentric rings divulging to its MNPs polycrystalline nature. The SAED diffraction rings secured for bare shell (F) and core (CZ) samples disposed of in Fig. 4a,b authenticate to their respective crystal plane orientation complementing the XRD analysis. Further, the SAED spectra survey for the CS sample CZF expressed in Fig. 4c distinctly disclosed the coexistence of both the crystal planes of core and shell samples. The electron diffraction rings perceived owing to planes (311) and (620) communicate to shell material F. However, the concentric rings on account to crystal planes (511) and (840) correspond to C material, while the rings due to crystallographic planes (220) and (731) are owing to Z material of the core sample CZ, which reflects authentically to XRD results.

An extensive inspection to morphology of the samples were further carried out by engaging FESEM, where the visualized morphology images of F, CZ, and CZF samples are shown in Fig. 5a–c, respectively. As displayed in the figures, an agglomeration is slightly revealed for all the samples exhibiting a spheroids shape particles similar to the images obtained from TEM analysis. The presently observed morphologies of F and CZ samples are identical to the morphology of the previously reported literature for the same synthesis method employed^{29,30}. The average particle diameter observed through the FESEM analysis for F, CZ, and CZF samples are respectively 15.32 ± 2 nm, 12.76 ± 3 nm, and 18.21 ± 2 nm. The sequence of particle sizes obtained from FESEM examinations is in concurrence with the TEM result. The enlargement particle size secured for the CS CZF sample might regard to the fine growth of F nanoparticles as a shell on the surface of the core CZ material.

The elemental composition of all the respective samples was detected utilizing an energy dispersive X-ray (EDX) analysis, where the corresponding spectra along with their elemental composition ratio in terms of atomic and weight percentage (%) are depicted in Fig. 6a–c. The peaks observed in Fig. 6a are on account of elements Fe and O which authenticate the origination of pure F crystal. Also, the EDX peaks perceived in Fig. 6b are divulging for elements Fe, O, Co and Zn respectively, revealing the emergence of a pure CZ material. The elemental component acquired in Fig. 6c for the CZF sample is identical to that of the CZ sample. However, the elemental proportion ratio in weight% and atomic% are unlike as visualized in the figure. The enhanced component of Fe elements achieved for the CS CZF sample might regard to the presence of F material as a shell component in the CS sample. The elemental composition ratio in % observed for all the samples are commensurate to the experimental anticipated % which is evident that the disappearance of elements is not discerning during synthesis.

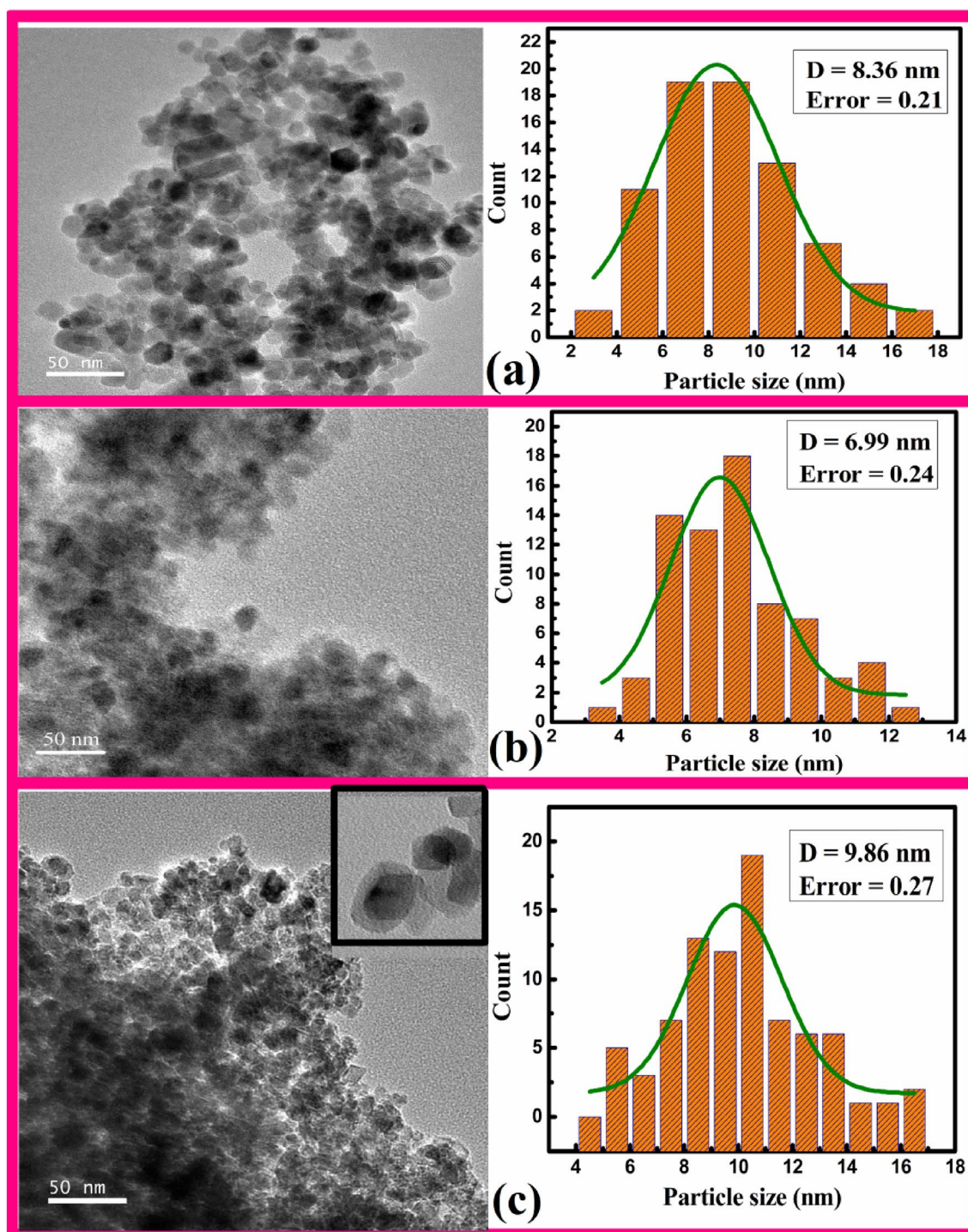


Figure 2. TEM micrograph with average particle size plotted histogram of (a) F, (b) CZ, and (c) CZF MNPs.

FTIR analysis. Figure 7 unveiled the FTIR spectroscopy analysis recorded at the 400–4000 cm^{-1} range to recognize the distinct vibrational characteristics of the lattice absorption bands for F, CZ, and CZF, respectively. As displayed in Fig. 7, all the distinct characteristic peaks for bare samples F and CZ are present at the CS sample CZF except that a slight shifting is recorded for the same. The probable reason leading to the shifting of peak position for CS CZF might accredit to the substitution of cobalt ions with Fe ions appearing in the octahedral sites, noting that the ions have unlike atomic mass and ionic radii³¹. Usually, the absorption bands exhibiting below 1000 cm^{-1} correspond to spinel ferrite features attributing to metal–oxygen (M–O) stretching vibrations^{32,33}. The absorption peak spotted at 539.28 cm^{-1} for the F sample is allocated to the stretching vibrations of Fe^{2+} and O^{2-} ions. Also, the two strong IR bands perceive around 400–500 cm^{-1} and 500–600 cm^{-1} for both CZ and CS CZF samples corresponding to intrinsic M–O stretching vibrations in the tetrahedral and

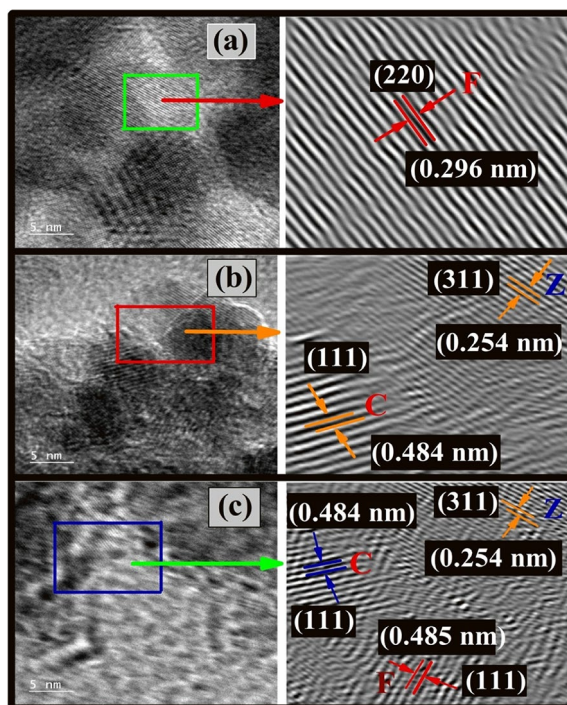


Figure 3. HRTEM image with IFFT lattice planes micrographs of (a) F, (b) C, and (c) CZF MNPs.

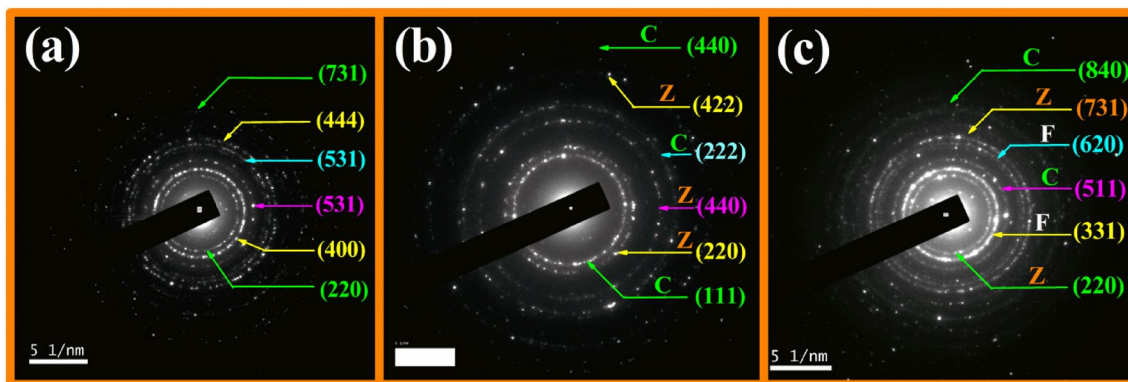


Figure 4. SAED pattern of (a) F, (b) CZ, and (c) CZF MNP.

octahedral sites^{34–36}. Therefore, the recorded IR peaks corresponding to M–O vibration modes divulge the origination of spinel ferrite cubic NPs.

Magnetic study. The magnetic quantification of MNP over applied field and temperature were examined through Physical Properties Measurement Systems (PPMS) and the emanated outcomes are depicted in Fig. 8a–c. The M–H loops perceived at room temperature (300 K) for single materials F and CZ are manifested in Fig. 8a,b, while the M–H hysteresis loops acquired for CS CZF sample at five distinct temperatures (60 K, 150 K, 200 K, 250 K and 300 K) are shown in Fig. 8c. The saturation magnetization (M_S) for samples F, CZ, and CZF at room temperature is achieved at about 57.34 emu/g, 27.89 emu/g, and 52.65 emu/g, respectively. The M_S value for the CS CZF sample is a joint benefaction made by both CZ (core) and F (shell) samples. However, the value leans more towards the F value which might be attributed to the more magnetic contribution made by the shell material. Interestingly, other magnetic parameters such as coercivity (H_C) and retentivity (M_R) follow the same fashion for the CS CZF sample over bare F and CZ samples. Thus, the outcome proclaims that the core and shell materials are coupled magnetically at their junction interface^{28,37,38}. The magnetic anisotropy (K_C) of F, CZ, and CZF samples were appraised by employing the law of approach fitting through initial magnetization curves³⁹. All the magnetic parameters perceived at room temperature are specified in Table 2. A low-temperature survey on the M–H loop was further employed for the CS CZF sample, for which an enhancement to saturation magnetization and coercivity is apparent at lowering the temperature. This implies that more

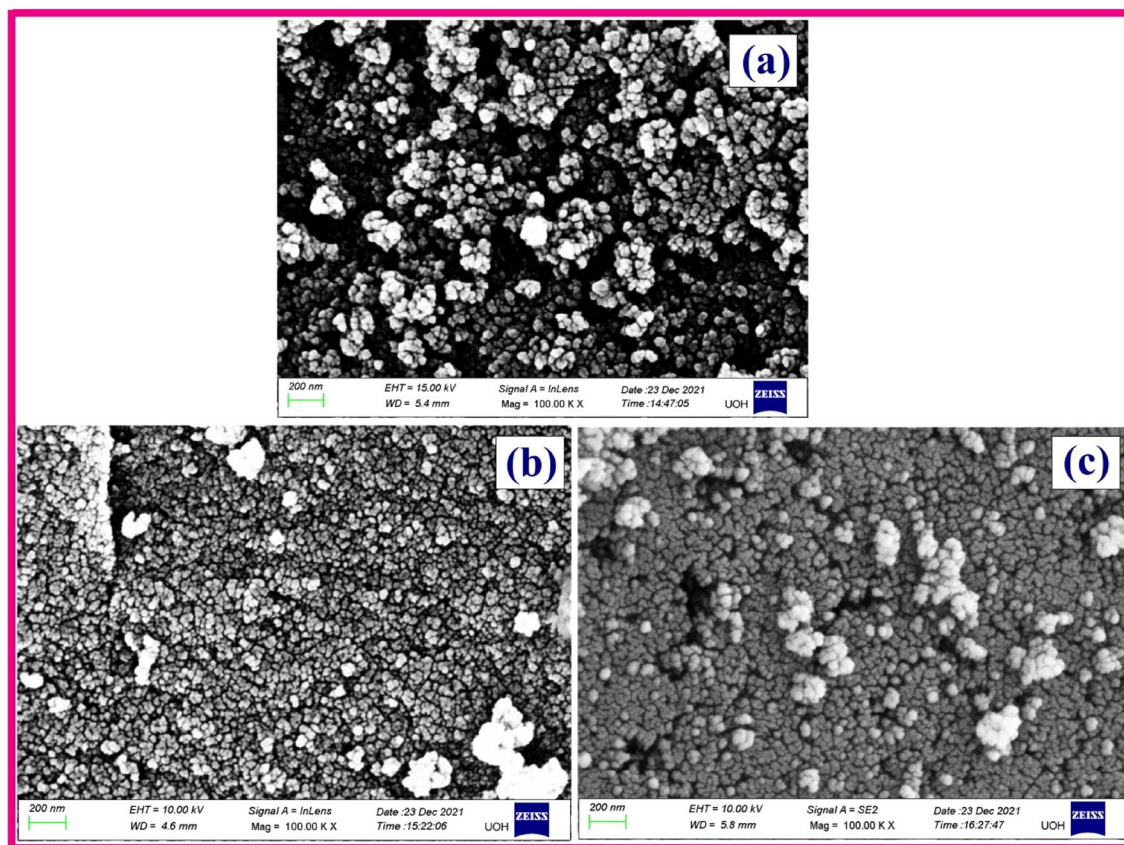


Figure 5. FESEM micrographs of (a) F, (b) CZ, and (c) CZF MNP.

magnetic moments tend to orient along the applied field attributing to more dominance of the magnetic field over temperature^{38,40}. To the utmost interest, the inflation in the M_S and H_C at lowering temperature is also escorted by loop relocation along the negative axis ascribing to the phenomenon of EBE. Generally, the relocation of the hysteresis loop originates as a consequence of induced unidirectional anisotropy engender through the interface exchange coupling between the core and shell materials^{41,42}. Although, the macroscopic origin of EBE exists for more than 50 years and despite its vital implementation in multiple applications, the microscopic behavior or its coupling mechanism is yet to fully recognize, which is still a debated field of interest. However, it is definitive that the EBE arises solely due to a small fraction of spins adheres at the interface layer of the core and shell materials despite its different combinations of core and shell systems (i.e. a system composed of Ferro/ferri-magnetic@anti-ferromagnetic, anti-ferromagnetic@ferro/ferri-magnetic, Ferro/ferri-magnetic@ferro/ferri-magnetic, etc.). It was experimentally evinced by Ohldag et al. that the induced unidirectional anisotropy generated through interface coupling is out-turn significant by a very small fraction less than about 4% of aligned interfacial spins at the junction of core and shell layer⁴³. Therefore, the consequence of such frustrated spins might have been initiated through the frozen spins at the interface which might be the factor responsible for the interface exchange anisotropy (EBE), although it provides very few donations towards the total magnetization. Also, one should take note that, under field cooling, the uncompensated spins at the interface surface and shell layer which are pinned to alignment are other factors guiding to EBE phenomenon. When the interfacial spins are pinned, it will require a large amount of Zeeman energy to orient along its direction, and therefore, in an attempt to neutralize the system, a negative intrinsic field is generated leading to the relocation of the M-H loop along the negative axis. For the present samples, the minimum temperature employed to investigate the M-H loop is 60 K. However, EBE is authenticating even at 60 K perceiving its maximum value as compared to the observation made at higher temperatures. The exchange bias field (H_{ex}) induced at 60 K is $H_{ex} = -10.34$ Oe and the value shrinks as we further surge the temperature. The minimum H_{ex} is noticed at 200 K ($H_{ex} = -3.94$ Oe) and no shifting is absolute at 250 K and 300 K. It is well understood that the shifting of the M-H loop usually fades away at the blocking temperature^{44,45}. Therefore, for further authentication, we have performed ZFC-FC measurement for the CS CZF sample at the cooling field of 100 Oe, where the plotting is displayed in Fig. 9. It is obvious from the figure that, the CZF sample perceived a blocking temperature of about 240 K which provides a complete picture of the non-existence of EBE at 250 K. Therefore, from the outcome resulted, it may be understood that more interfacial spins are pinned to alignment at lower temperature directing to higher H_{ex} . However, as the temperature gets enhanced, the thermal energy suppresses the local anisotropy and allows the interfacial spins to an easier orientation towards the field direction, thus producing hindrance to EBE, which

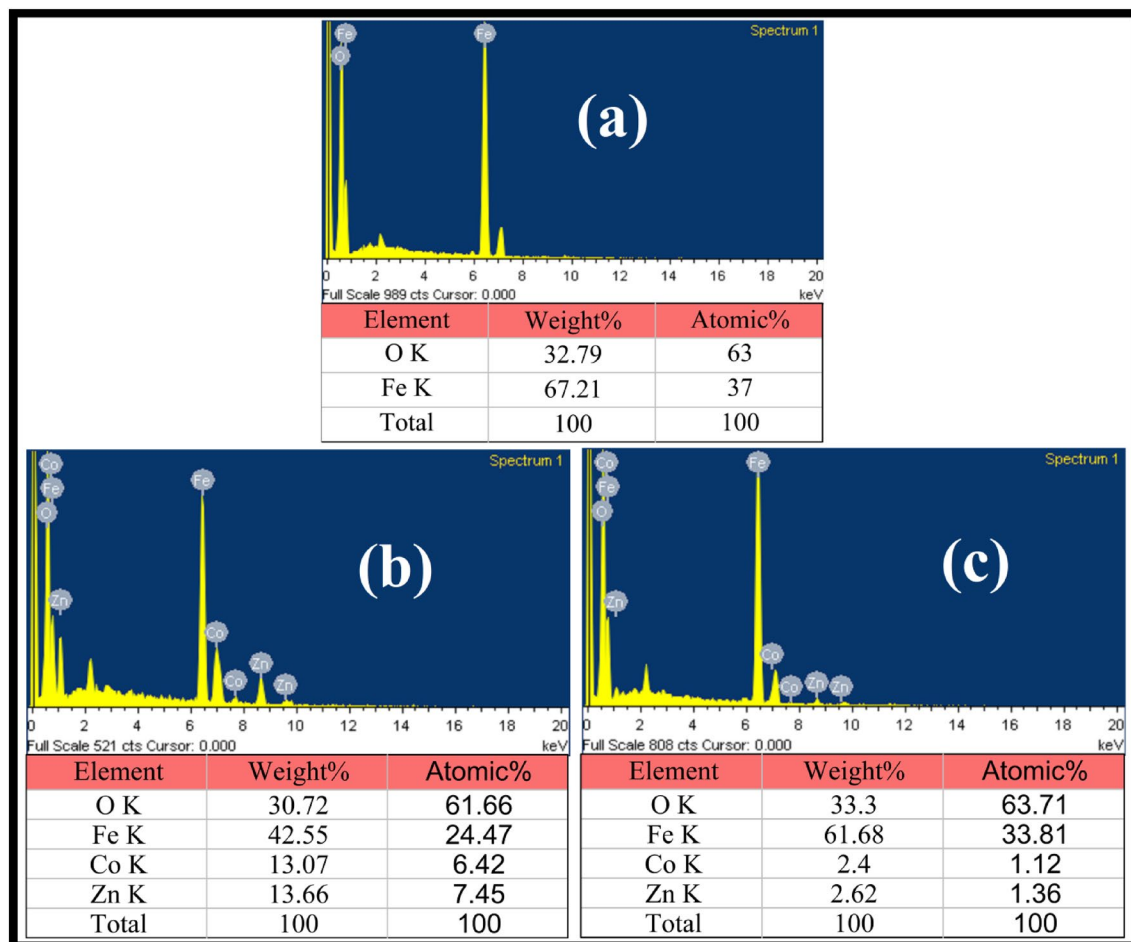


Figure 6. EDX patterns of (a) F, (b) CZ, and (c) CZF samples.

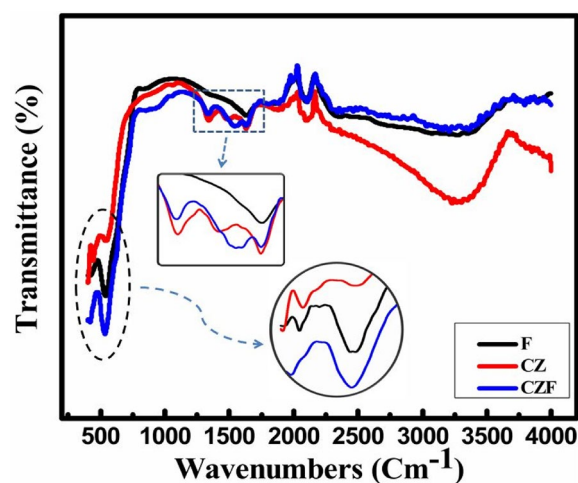


Figure 7. FTIR transmission spectra for F, CZ, and CZF samples.

finally disappears at the blocking temperature and beyond which no relocation is evident. The magnetic properties of CS CZF at lower temperatures are designated in Table 3.

Induction study. The rate of temperature inflation with time for the MNP was analyzed employing an easy heat 8310 (Ambrell make UK) having 7 and 8 turns of diameter coils dispatched at three distinct fields i.e. 12.38 kAm^{-1} , 13.92 kAm^{-1} and 15.47 kAm^{-1} and conventional frequency ($f=337 \text{ MHz}$) for samples CZ, F, and

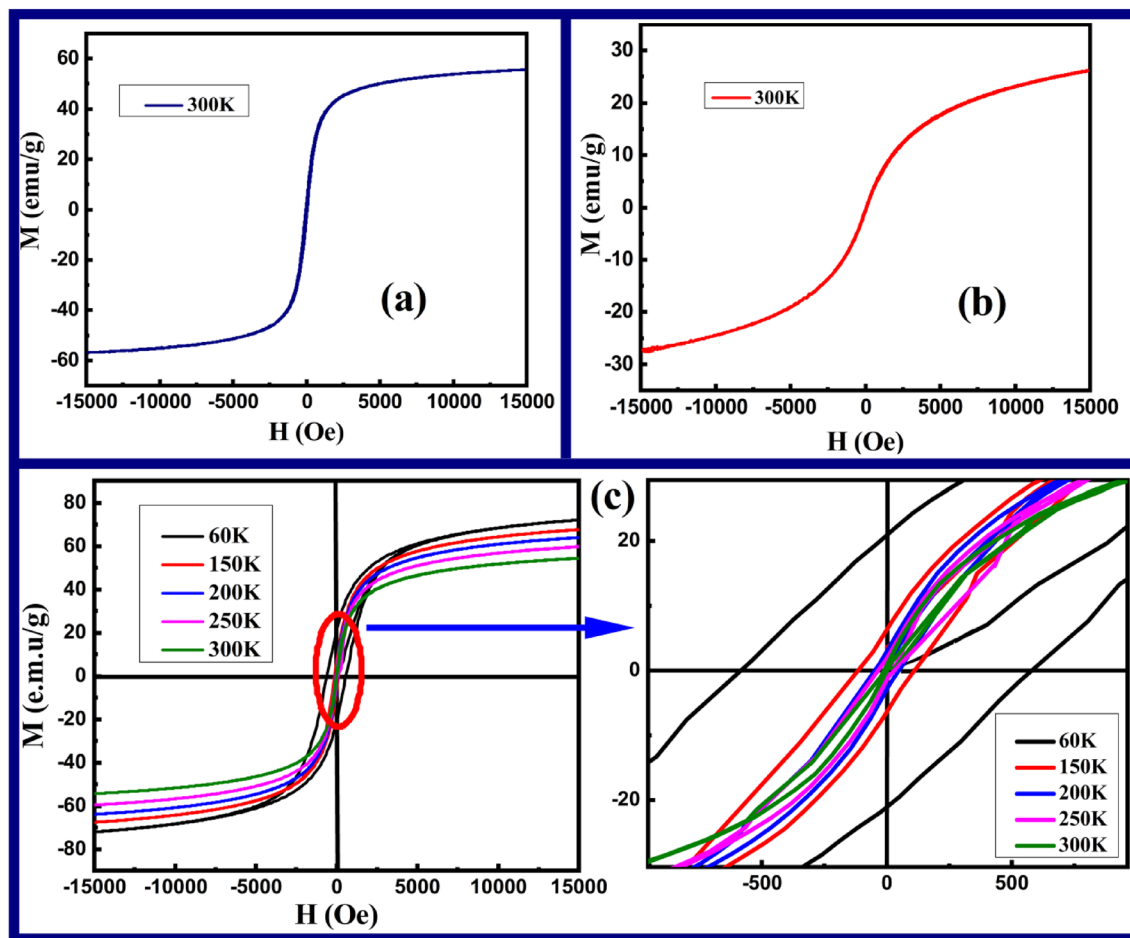


Figure 8. Magnetic hysteresis loop (a) at 300 K for F, (b) at 300 K for CZ samples, and (c) five distinct temperatures for CS CZF sample.

Sample	M_S (emu/g)	M_R (emu/g)	H_C (Oe)	M_R/M_S	K_C ($\times 10^4$ Jm $^{-3}$)
F	57.34	3.21	50.14	0.055	4.87
CZ	27.89	0.18	21.48	0.006	1.69
CZF	52.65	1.31	37.25	0.032	3.42

Table 2. Magnetic parameters for F, CZ, and CZF samples at 300 K.

CZF, respectively. This particular investigation is carried out to recognize the heat generation potential of the MNP which is quantified to a specific loss power (SLP). The prime objective is to acquire supreme SAR value with the least sample concentration within the clinical safety restraint called Brezovich limit⁹ i.e. the multiplication of frequency and the applied field should not surpass $\approx 5 \times 10^9$ Am $^{-1}$ s $^{-1}$. In our study, the multiplication of frequency and the distinct applied fields ($H \times f$) falls in less than the clinical restraint; thus satisfying one of the foremost requirement for hyperthermia applications. To optimize the heating perspective of the MNP, 1 mg mass of each sample (CZ, F, and CZF) were solvated in 1 mL Milli Q water which is further placed within the work-coil. Then the sample is placed in AC magnetic field with the particular amplitude and frequency, where the fibre optics temperature probe simultaneously records the temperature rise of the sample with respect to time for about 15 min (900 s) for all the three distinctive applied fields, where their respective results yielded are illustrated in Fig. 10a–c. An air cooled insulation and polyurethane coil was used between the nanoparticles tube and induction coil in order to secure the nanoparticles in being heated up by residual heat through the induction coil. The heating potential or the SLP value prevailed through a non-adiabatic setup, where the curve is contoured manoeuvring the Box–Lucas (B–L) equation^{46,47}. It is noticed that the CZ sample does not acquire the hyperthermia threshold temperature (42–46 °C) even for the measurement recorded at 15.47 kAm $^{-1}$ field. The impotence to acquiring threshold temperature for the CZ sample might regard to its low anisotropy energy and low saturation magnetization⁴⁸. Sample F being associated with the highest saturation magnetization and anisotropy energy achieved the temperature requirement within 900 s for all the respective fields. Interestingly, the CS CZF sample executed to threshold temperature within 500 s despite its lower magnetic response

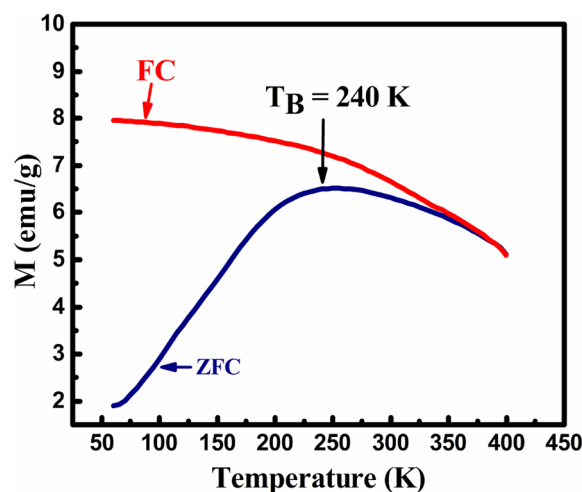


Figure 9. ZFC–FC plot at 100 Oe for CS CZF sample.

Temperature	M_S (emu/g)	M_R (emu/g)	H_C (Oe)	M_R/M_S	H_{ex} (Oe)
250 K	63.11	2.12	42.55	0.034	–
200 K	67.70	2.61	49.23	0.039	–3.94
150 K	71.96	6.4	113.21	0.089	–5.83
60 K	76.23	21.16	582.49	0.278	–10.34

Table 3. Magnetic properties of CS CZF sample for different temperatures.

compared to F materials. This outcome manifests that more heat dissipation prevailed for CZF MNP. The probable reason behind this output could be related to the EBE phenomenon resulting from the exchange coupling at the interface junction of the core and shell materials, where the benefaction of this additional interface exchange anisotropy energy eccentrically tunes the effective anisotropy of CZF sample^{49–51}. The wielding of suitable shell material with appropriate thickness is another prime component in magnifying the surface anisotropy which is an additional endowment to the total effective anisotropy. Moon et al. experimentally delineate that, Fe_3O_4 with a thin shell to about $\approx 1\text{--}2$ nm plays a crucial part to enhance the surface anisotropy that contributes to the higher heating capability of the MNP⁵². The SLP values secured at 12.38 kAm^{-1} field are 43.79 W/g , 160.59 W/g , and 276.08 W/g for the corresponding samples CZ, F, and CZF, respectively. The inflation on the applied magnetic field will pilot the magnetic spins to more fluctuations that will engender lofty heat dissipation of the MNP. Consequently, the highest SLP value is secured for the measurement drawn at 15.47 kAm^{-1} field for the CS CZF sample which is acquired to about 340.85 W/g . It is also supreme to obtain a normalized value for the corresponding SLP values through the removal of the extrinsic parameters since the power inception of the MNP scales linearly with the frequency and quadratically to the magnetic field applied, which is regarded as intrinsic loss power (ILP)^{53,54}. The calculated ILP values and the corresponding SLP values for all the respective currents are prescribed in Table 4. It is also cardinal to note that, the typical ILP values reported in the earlier literature^{55–58} for suitable heating take a value ranging between 3 and $4\text{ nHm}^2\text{ g}^{-1}$. Our perceived ILP values for the CS CZF sample are beyond $4\text{ nHm}^2\text{ g}^{-1}$, with the highest recorded for 12.38 kAm^{-1} field which is about $5.36\text{ nHm}^2\text{ g}^{-1}$ remarking as a suitable agent with high heating capability. Also, as shown in Fig. 10, on removal of the applied magnetic field, the nanoparticles cooled down to its initial temperature taking just about 10 min approximately.

Therefore; based on the MNP heating retaliations, it may be pointed out that for the CS CZF sample, the employment of befitting shell material with suitable thickness amplifies the surface anisotropy and the manifestation of extra interface exchange anisotropy as a consequence of the EBE through the junction interface coupling had significantly modulated the effective anisotropy, thus directing to the superior heating capability of the CS sample. Hence, it is commended that a core@shell type nanostructure is genuinely prominent to effectively revamp the heating capability of the MNP, and therefore, the CS CZF sample is marked to be a desirable emissary to effectual magnetic hyperthermia applications.

Conclusion

CZ, F, and CS CZF MNP samples were meticulously prepared by utilizing a co-precipitation course of action, where the investigation on its microstructure, morphology, and magnetic behavior was carried out employing an XRD, FESEM, HRTEM, and VSM, respectively. The origination of CS nanostructure is apparent through the TEM micrograph, where a slightly agglomerated spheroids MNP is visualized through the FESEM and TEM micrographs. A lattice plane authentication through the HRTEM study further confirmed the core and shell

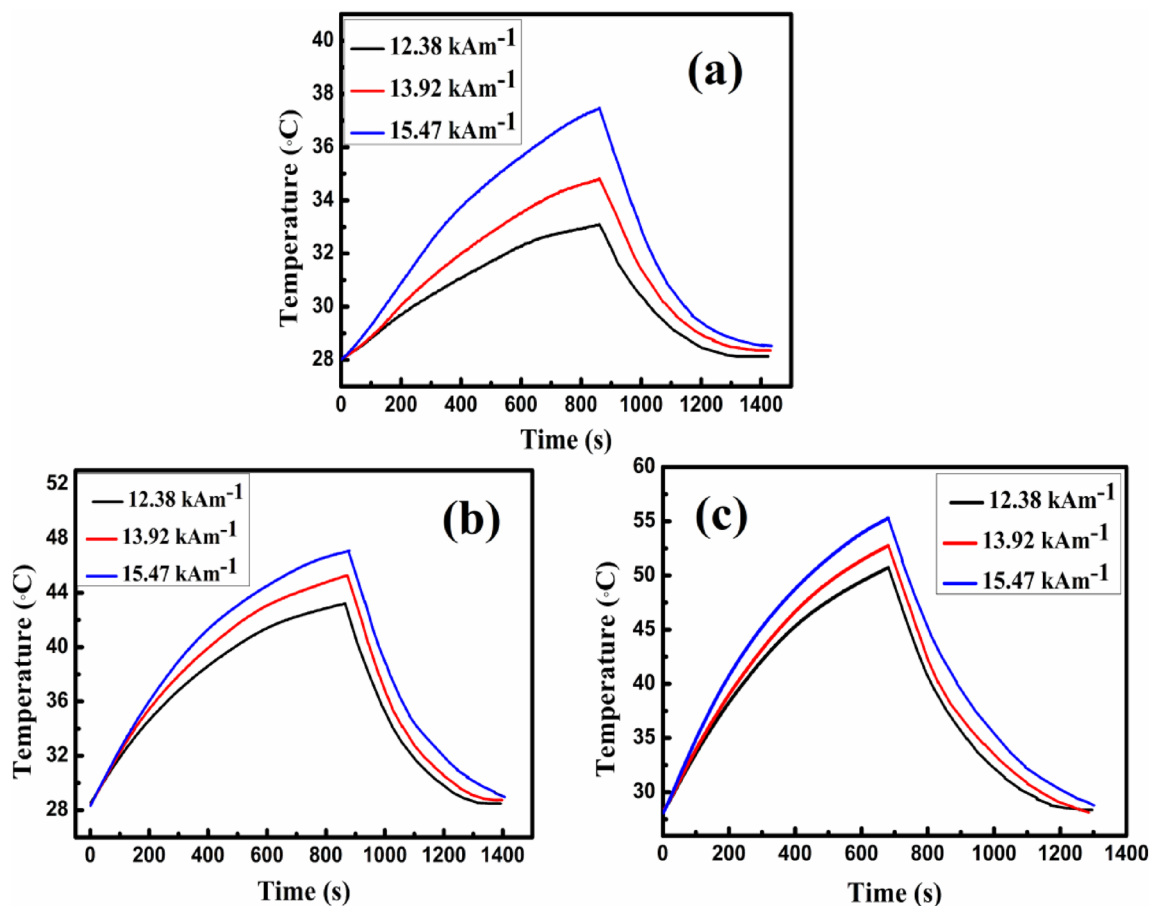


Figure 10. Heat dissipation with time and cooling curve for (a) CZ, (b) F, and (c) CZF MNPs at three different fields.

Samples	SLP (W/g) for 1 mg			ILP $\times 10^{-3}$ (nHm ² g ⁻¹)		
	12.38 kAm ⁻¹	13.92 kAm ⁻¹	15.47 kAm ⁻¹	12.38 kAm ⁻¹	13.92 kAm ⁻¹	15.47 kAm ⁻¹
CZ	43.79	56.02	81.88	0.85	0.86	1.01
F	160.59	185.99	218.48	3.12	2.96	2.61
CZF	276.08	289.71	340.85	5.36	4.45	4.24

Table 4. Values of ILP and SAR at three different fields for all the samples.

materials, where their elemental compositions are divulged employing an EDX. The VSM appraisal disclosed a relocation of the hysteresis loop (EBE) for the CS CZF sample, substantiating to strong exchange interaction between the core and shell materials. It is also validated that, the EBE fades away at the blocking temperature ($T_B = 240$ K). Intriguingly, magnetic response to saturation magnetization and anisotropy is higher for the F sample; however, the heat liberated by the CS CZF MNP was outrageously amplified compared to both CZ and F samples reaching hyperthermia threshold temperature within 500 s. The credible reason behind this astonishing consequence might regard to the usage of appropriate soft shell material with a befitting thickness that remarkably ameliorates the surface anisotropy and also, the significant outcome of EBE legitimating to hefty exchange coupling at the interface of the core and shell materials bestowing to extra interface exchange anisotropy, which consequentially tuned the effective anisotropy of the CS CZF sample. A notably high SLP value of about 340.85 W/g with a lofty ILP value is attained for the CS sample. Therefore, CS nanostructure with astonishing interface coupling phenomenon (EBE) is conspicuous to intensify the heating ability of the MNP, and hence, the CS CZF sample is a prominent agent to contrivance on magnetic hyperthermia applications.

Data availability

The datasets generated and/or analyzed during the current study are available in the crystallographic open database repository, [COD ID: 1010369 and 1010130].

Received: 6 April 2023; Accepted: 30 July 2023

Published online: 22 August 2023

References

- Shabatina, T. I., Vernaya, O. I., Shabatin, V. P. & Melnikov, M. Y. Magnetic nanoparticles for biomedical purposes: Modern trends and prospects. *Magnetochemistry* **6**, 30 (2020).
- Williams, H. M. The application of magnetic nanoparticles in the treatment and monitoring of cancer and infectious diseases. *Biosci. Horizons Int. J. Stud. Res.* **10**, 1–10 (2017).
- Giustini, A. J. *et al.* Magnetic nanoparticle hyperthermia in cancer treatment. *Nano Life* **01**, 17–32 (2010).
- Gilchrist, R. K. *et al.* Selective inductive heating of lymph nodes. *Ann. Surg.* **146**, 596–606 (1957).
- Beik, J. *et al.* Nanotechnology in hyperthermia cancer therapy: From fundamental principles to advanced applications. *J. Control. Release* **235**, 205–221 (2016).
- Tsopoe, S. P., Borah, J. P. & Borgohain, C. An investigation of mixed spinel ferrite $\text{Co}_{0.5}\text{Zn}_{0.5}\text{Fe}_2\text{O}_4$ nanoparticles for effective magnetic fluid hyperthermia applications. *Mater. Today Proc.* **68**, 163–166 (2022).
- Maier-Hauff, K. *et al.* Efficacy and safety of intratumoral thermotherapy using magnetic iron-oxide nanoparticles combined with external beam radiotherapy on patients with recurrent glioblastoma multiforme. *J. Neurooncol.* **103**, 317–324 (2011).
- Kumar, C. S. S. R. & Mohammad, F. Magnetic nanomaterials for hyperthermia-based therapy and controlled drug delivery. *Adv. Drug Deliv. Rev.* **63**, 789–808 (2011).
- Hergt, R., Dutz, S., Müller, R. & Zeisberger, M. Magnetic particle hyperthermia: Nanoparticle magnetism and materials development for cancer therapy. *J. Phys. Condens. Matter* **18**, S2919–S2934 (2006).
- Jamir, M., Islam, R., Pandey, L. M. & Borah, J. P. Effect of surface functionalization on the heating efficiency of magnetite nanoclusters for hyperthermia application. *J. Alloys Compd.* **854**, 157248 (2021).
- Hilger, I. In vivo applications of magnetic nanoparticle hyperthermia. *Int. J. Hyperth.* **29**, 828–834 (2013).
- Rocho-Pérez, J. A. *et al.* A full set of in vitro assays in chitosan/tween 80 microspheres loaded with magnetite nanoparticles. *Polymers (Basel)*. **13**, 1–15 (2021).
- El-Gendy, A. A. Core/shell magnetic nanoparticles for biomedical applications. In *Magnetic Nanostructured Materials* 41–58 (Elsevier, 2018). <https://doi.org/10.1016/B978-0-12-813904-2.00002-4>.
- Meiklejohn, W. H. & Bean, C. P. New magnetic anisotropy. *Phys. Rev.* **102**, 1413–1414 (1956).
- Nogués, J. & Schuller, I. K. Exchange bias. *J. Magn. Magn. Mater.* **192**, 203–232 (1999).
- González, J. A. *et al.* Maximizing exchange bias in co/coo core/shell nanoparticles by lattice matching between the shell and the embedding matrix. *Chem. Mater.* **29**, 5200–5206 (2017).
- Borgohain, C., Mishra, D., Sarma, K. C. & Phukan, P. Exchange bias effect in CoFe_2O_4 - Cr_2O_3 nanocomposite embedded in SiO_2 matrix. *J. Appl. Phys.* **112**, 113905 (2012).
- Skumryev, V. *et al.* Beating the superparamagnetic limit with exchange bias. *Nature* **423**, 850–853 (2003).
- Tsopoe, S. P., Borgohain, C., Fopase, R., Pandey, L. M. & Borah, J. P. A comparative investigation of normal and inverted exchange bias effect for magnetic fluid hyperthermia applications. *Sci. Rep.* **10**, 18666 (2020).
- Robles, J., Das, R., Glassell, M., Phan, M. H. & Srikanth, H. Exchange-coupled $\text{Fe}_3\text{O}_4/\text{CoFe}_2\text{O}_4$ nanoparticles for advanced magnetic hyperthermia. *AIP Adv.* **8**, 056719 (2018).
- Nandwana, V. *et al.* Exchange coupling in soft magnetic nanostructures and its direct effect on their theranostic properties. *ACS Appl. Mater. Interfaces* **10**, 27233–27243 (2018).
- Garaio, E. *et al.* Specific absorption rate dependence on temperature in magnetic field hyperthermia measured by dynamic hysteresis losses (ac magnetometry). *Nanotechnology* **26**, 015704 (2015).
- Mohapatra, J. *et al.* Size-dependent magnetic and inductive heating properties of Fe_3O_4 nanoparticles: Scaling laws across the superparamagnetic size. *Phys. Chem. Chem. Phys.* **20**, 12879–12887 (2018).
- Lima, E. *et al.* Size dependence of the magnetic relaxation and specific power absorption in iron oxide nanoparticles. *J. Nanopart. Res.* **15**, 1654 (2013).
- Yüksel, Y. Effects of the particle size and shape of the magnetic nanoparticles on the magnetic hyperthermia and exchange bias properties. *Phys. B Condens. Matter* **575**, 411689 (2019).
- Patterson, A. L. The Scherrer formula for X-ray particle size determination. *Phys. Rev.* **56**, 978–982 (1939).
- Singer, A., Barakat, Z., Mohapatra, S. & Mohapatra, S. S. Nanoscale drug-delivery systems. In *Nanocarriers for Drug Delivery* 395–419 (Elsevier, 2019). <https://doi.org/10.1016/B978-0-12-814033-8.00013-8>.
- Lavorato, G. *et al.* Bifunctional $\text{CoFe}_2\text{O}_4/\text{ZnO}$ core/shell nanoparticles for magnetic fluid hyperthermia with controlled optical response. *J. Phys. Chem. C* **122**, 3047–3057 (2018).
- Davar, F., Majedi, A. & Abbasi, A. Synthesis of $\text{Fe}_3\text{O}_4@ZrO_2$ core-shell nanoparticles through new approach and its solar light photocatalyst application. *J. Mater. Sci. Mater. Electron.* **28**, 4871–4878 (2017).
- Manikandan, A., Kennedy, L. J., Bououdina, M. & Vijaya, J. J. Synthesis, optical and magnetic properties of pure and Co-doped ZnFe_2O_4 nanoparticles by microwave combustion method. *J. Magn. Magn. Mater.* **349**, 249–258 (2014).
- Jamil, M. T. *et al.* Effect on structural and optical properties of Zn-substituted cobalt ferrite $\text{Co}_2\text{Fe}_2\text{O}_4$. *J. Ovonic Res.* **13**, 45–53 (2017).
- Borade, R. M., Somvanshi, S. B., Kale, S. B., Pawar, R. P. & Jadhav, K. M. Spinel zinc ferrite nanoparticles: An active nanocatalyst for microwave irradiated solvent free synthesis of chalcones. *Mater. Res. Express* **7**, 016116 (2020).
- Nouri, A. *et al.* Synthesis and characterization of cobalt zinc ferrite-chitosan core-shell nanoparticles. **2**, 16–20 (2014).
- Jandl, S. & Deslandes, J. Infrared spectra of ferrites. *Phys. Rev. B* **24**, 1040–1044 (1981).
- Deshmukh, S. S., Humbe, A. V., Kumar, A., Dorik, R. G. & Jadhav, K. M. Urea assisted synthesis of $\text{Ni}_{1-x}\text{Zn}_x\text{Fe}_2\text{O}_4$ ($0 \leq x \leq 0.8$): Magnetic and Mössbauer investigations. *J. Alloys Compd.* **704**, 227–236 (2017).
- Borhan, A. I., Iordan, A. R. & Palamaru, M. N. Correlation between structural, magnetic and electrical properties of nanocrystalline Al^{3+} substituted zinc ferrite. *Mater. Res. Bull.* **48**, 2549–2556 (2013).
- Honarbaksh-Raouf, A., Emamian, H. R., Yourdkhani, A. & Ataie, A. Synthesis and characterization of $\text{CoFe}_2\text{O}_4/\text{Ni}_{0.5}\text{Zn}_{0.5}\text{Fe}_2\text{O}_4$ core/shell magnetic nanocomposite by the wet chemical route. *Int. J. Mod. Phys. B* **24**, 5807–5814 (2010).
- Tajyani, S. & Babaei, A. A new sensing platform based on magnetic $\text{Fe}_3\text{O}_4/\text{NiO}$ core/shell nanoparticles modified carbon paste electrode for simultaneous voltammetric determination of Quercetin and Tryptophan. *J. Electroanal. Chem.* **808**, 50–58 (2018).
- Brown, W. F. Theory of the approach to magnetic saturation. *Phys. Rev.* **58**, 736–743 (1940).
- Caizer, C. & Hrianca, I. The temperature dependence of saturation magnetization of $\gamma\text{-Fe}_2\text{O}_3/\text{SiO}_2$ magnetic nanocomposite. *Ann. Phys.* **12**, 115–122 (2003).
- Tracy, J. B. & Bawendi, M. G. Defects in CoO in oxidized cobalt nanoparticles dominate exchange biasing and exhibit anomalous magnetic properties. 1–11 (2006) <https://doi.org/10.1103/PhysRevB.74.184434>.
- Ali, M. *et al.* Exchange bias using a spin glass. *Nat. Mater.* **6**, 2–7 (2007).
- Ohldag, H. *et al.* Correlation between exchange bias and pinned interfacial spins. *Phys. Rev. Lett.* **91**, 017203 (2003).
- Gandha, K., Chaudhary, R. P., Mohapatra, J., Koymen, A. R. & Liu, J. P. Giant exchange bias and its angular dependence in Co/CoO core-shell nanowire assemblies. *Phys. Lett. A* **381**, 2092–2096 (2017).

45. Kavich, D. W., Dickerson, J. H., Mahajan, S. V., Hasan, S. A. & Park, J.-H. Exchange bias of singly inverted FeO/Fe₃O₄ core-shell nanocrystals. *Phys. Rev. B* **78**, 174414 (2008).
46. Teran, F. J. *et al.* Accurate determination of the specific absorption rate in superparamagnetic nanoparticles under non-adiabatic conditions. *Appl. Phys. Lett.* **062413**, 2010–2014 (2014).
47. Seal, P. *et al.* Optimization of self heating properties of Fe₃O₄ using PEG and amine functionalized MWCNT. *J. Alloys Compd.* **882**, 160653 (2021).
48. Kahmei, R. D. R. Nanoscale advances tunable heat generation in nickel-substituted zinc ferrite nanoparticles for magnetic hyperthermia †. *Nanoscale Adv.* **00**, 1–9 (2021).
49. Vamvakidis, K. *et al.* Magnetic hyperthermia efficiency and MRI contrast sensitivity of colloidal soft/hard ferrite nanoclusters. *J. Colloid Interface Sci.* **511**, 101–109 (2018).
50. Phadatare, M. R., Meshram, J. V., Gurav, K. V., Kim, J. H. & Pawar, S. H. Enhancement of specific absorption rate by exchange coupling of the core-shell structure of magnetic nanoparticles for magnetic hyperthermia. *J. Phys. D. Appl. Phys.* **49**, 095004 (2016).
51. Park, J., Choi, H., Kim, S. J. & Kim, C. S. Examination of the magnetic hyperthermia and other magnetic properties of CoFe₂O₄@MgFe₂O₄ nanoparticles using external field Mössbauer spectroscopy. *AIP Adv.* **8**, 056113 (2018).
52. Moon, S. H. *et al.* Ultrathin interface regime of core-shell magnetic nanoparticles for effective magnetism tailoring. *Nano Lett.* <https://doi.org/10.1021/acs.nanolett.6b04016> (2017).
53. Kallumadil, M. *et al.* Suitability of commercial colloids for magnetic hyperthermia. *J. Magn. Magn. Mater.* **321**, 1509–1513 (2009).
54. He, S. *et al.* Maximizing specific loss power for magnetic hyperthermia by hard-soft mixed ferrites. *Small* **14**, 1800135 (2018).
55. Cao, J. *et al.* Iodinated-cyanine dyes for fast NIR-guided deep-tissue synergistic phototherapy. *ACS Appl. Mater. Interfaces* <https://doi.org/10.1021/acsami.9b07694> (2019).
56. Iqbal, Y., Bae, H. & Rhee, I. Control of the saturation temperature in magnetic heating by using polyethylene-glycol-coated rod-shaped nickel-ferrite (NiFe₂O₄) nanoparticles. *J. Korean Phys. Soc.* **68**, 587–592 (2016).
57. Sakellari, D., Simeonidis, K., Angelakeris, M. & Dendrinou-samara, C. Tunable AC magnetic hyperthermia efficiency of Ni ferrite nanoparticles. *IEEE Trans. Magn.* <https://doi.org/10.1109/TMAG.2014.2345637> (2014).
58. Lasheras, X. *et al.* Chemical synthesis and magnetic properties of monodisperse nickel ferrite nanoparticles for biomedical applications. *J. Phys. Chem. C* <https://doi.org/10.1021/acs.jpcc.5b10216> (2016).

Acknowledgements

We thank the central instrumental facility (CIF), IIT Guwahati for granting us to utilize the instrumental facilities. We also thank prof. S Srinath and his team (School of Physics, University of Hyderabad), for their kind help on the FESEM characterization.

Author contributions

S.P.T. and J.P.B. have analyzed the samples and also prepared most of the contents on the manuscript. C.B. have done the HRTEM characterization and also prepared some portions of the manuscript. M.K. and S.K. have carried out the magnetic characterization and wrote some portions of the manuscript. All the authors have reviewed the manuscript.

Competing interests

The authors declare no competing interests.

Additional information

Correspondence and requests for materials should be addressed to J.P.B.

Reprints and permissions information is available at www.nature.com/reprints.

Publisher's note Springer Nature remains neutral with regard to jurisdictional claims in published maps and institutional affiliations.



Open Access This article is licensed under a Creative Commons Attribution 4.0 International License, which permits use, sharing, adaptation, distribution and reproduction in any medium or format, as long as you give appropriate credit to the original author(s) and the source, provide a link to the Creative Commons licence, and indicate if changes were made. The images or other third party material in this article are included in the article's Creative Commons licence, unless indicated otherwise in a credit line to the material. If material is not included in the article's Creative Commons licence and your intended use is not permitted by statutory regulation or exceeds the permitted use, you will need to obtain permission directly from the copyright holder. To view a copy of this licence, visit <http://creativecommons.org/licenses/by/4.0/>.

© The Author(s) 2023